

3D-printed Polyether-ether ketone/Carboxymethyl Cellulose Scaffolds coated with Zn-Mn doped mesoporous bioactive glass nanoparticles

Awab Mughal^{1,2,#}, Syed Muneeb Haider Gillani^{1,2,#}, Sheraz Ahmed^{2,#}, Duaa Fatima^{2,4}, Rabia Hussain¹, Jawad Manzur¹, Muhammad Haseeb Nawaz², Badar Minhas¹, Muhammad Shoaib Butt⁴, Mahdi Bodaghi^{3,*}, Muhammad Atiq Ur Rehman^{1,2,*}

¹Centre of Excellence in Biomaterials and Tissue Engineering, Materials Science Engineering Department, Government College University, 54000, Lahore, Pakistan

²Department of Materials Science & Engineering, Institute of Space Technology, 44000, Islamabad, Pakistan

³Department of Engineering, School of Science and Technology, Nottingham Trent University, Nottingham NG11 8NS, UK.

⁴School of Chemical and Material Engineering (SCME), National University of Sciences and Technology (NUST), H-12, Islamabad, 44000 Pakistan

These authors contributed equally.

*Corresponding Authors: atique1.1@hotmail.com; mahdi.bodaghi@ntu.ac.uk

Abstract:

Patient-specific fabrication of scaffold/implant requires an engineering approach to fabricate the ideal scaffold. Herein, we design 3D printed scaffolds comprised of polyether-ether-ketone (PEEK) and sodium-carboxymethyl cellulose (Na-CMC). The fabricated scaffold was dip coated with Zn and Mn doped bioactive glass nanoparticles (Zn-Mn MBGNs). The synthesized ink exhibit suitable shear-thinning behavior for direct ink write (DIW) 3D printing. The scaffolds were crafted with precision, featuring 85% porosity, 0.3 mm layer height, and 1.5 mm/s printing speed at room temperature. Scanning electron microscopy images reveal a well-defined scaffold with an average pore size of $600 \pm 30 \mu\text{m}$. The energy dispersive X-ray spectroscopy analysis confirmed a well dispersed/uniform coating of Zn-Mn MBGNs on the PEEK/Na-CMC scaffold. Fourier transform infrared spectroscopy confirmed the presence of PEEK, CMC, and Zn-Mn MBGNs. The tensile test revealed a Young's modulus of 2.05 GPa. Antibacterial assays demonstrate inhibition zone against *Staphylococcus aureus* and *Escherichia Coli* strains. Chick Chorioallantoic

31 Membrane assays present significant angiogenesis, owe to the antigenic nature of Zn-Mn
32 MBGNs. WST-8 cell viability assays depicted cell proliferation, with a 103% viability after 7 days
33 of culture. This study suggests that the PEEK/Na-CMC scaffolds coated with Zn-Mn MBGNs
34 scaffolds are a candidate for osteoporotic fracture treatment. Thus, the fabricated scaffold can
35 offer multifaceted properties for enhanced patient outcomes in the bone tissue engineering.

36 **Keywords** — Additive Manufacturing (AM); 3D Bioprinting, Direct Ink Write (DIW);
37 Biomaterials; CMC; Polyetheretherketone (PEEK); Bioactive Glass Nanoparticles

38 1. Introduction

39 Bone defects pose a significant challenge in tissue engineering, especially in traumatic
40 injuries or surgical interventions. Biomaterials are pivotal, offering biocompatibility,
41 biodegradability, and osteointegration. Osteointegration, a permanent bond with living bone and
42 implants, requires superior biomaterials for osteoblast proliferation. However, issues like
43 corrosion and wear in commonly used metal materials need a substitution¹. The treatment of bone
44 defects is a global health problem, with current methods, such as metal implants, having drawbacks
45 like donor site morbidity, infection risk, and immunological responses. Traditional orthopedic
46 implants are used widely and have drawbacks such as a higher elastic modulus than bone, causing
47 additional stress and loosening of implants, etc.^{2,3}. Furthermore, they do not possess good
48 corrosion-resistance and are incompatible with imaging techniques like computed tomography
49 (CT) and magnetic resonance imaging (MRI), hindering monitoring of bone growth³.

50 Biopolymers offer biocompatible scaffolds for bone tissue engineering, promoting cell
51 adhesion and growth. Thermopolymers enhance scaffold mechanical strength and stability,
52 essential for load-bearing applications. The combination of both biopolymers and thermopolymers
53 provides a new platform, controlling the diverse needs of bone regeneration. Since various
54 polymers have been used for bone replacement⁴, but polyvinyl acrylate (PVA), polyhydroxy
55 butyrate (PHB), and polyether ether ketone (PEEK) are now widely used in orthopedics, providing
56 alternatives to metal implants^{5,6}. PEEK, a biocompatible polymer, has remarkable mechanical
57 properties and has been used in bone substitutes like intervertebral fusion devices^{7,8}.

58 Polyetheretherketone (PEEK) has been increasingly employed as an implant material in clinical
59 applications due to its biocompatibility, chemical stability, and radiolucency^{9,10}. It has an elastic
60 modulus similar to that of natural bone, which is a distinct advantage over metallic implants like
61 titanium that can contribute to stress shielding and the resorption of surrounding bone^{9,11,12}.
62 However, its biological inertness limits osteointegration, affecting long-term durability¹³. Despite
63 this, PEEK has biomechanical qualities similar to human bones, reducing the risk of bone
64 resorption caused by the stress-shielding effect of implants¹⁴.

65 Melting a polymer affects its microstructure leading to loss in mechanical properties like
66 stiffness and modulus of elasticity. At elevated temperatures loading of biomolecules and cells is
67 also a challenge. Direct Ink Write (DIW) or 3D-bioprinting is gaining interest in bone tissue
68 engineering. DIW is an extrusion-based 3D-printing method which prints near ambient
69 temperatures¹⁵. This helps to maintain the properties of the material, as it is not subjected to high
70 temperatures that could alter its characteristics. DIW allows precise control of scaffold geometry
71 and pore size, significant for bone regeneration¹⁶. It also enables high-resolution and precision
72 scaffolds, replicating the intricate microarchitecture of bone tissue^{17,18}.

73 Recent progress includes 3D-printed biphasic calcium phosphate (BCP) bioceramics,
74 improving mechanical characteristics and bone regeneration¹⁹. Researchers are focusing on novel
75 bone tissue engineering scaffolds with customized properties²⁰⁻²³. Additive manufacturing
76 techniques, like 3D printing, show advancements in bone tissue engineering²⁴. Interfaces between
77 bioceramics and biopolymers aim to improve both mechanical and biological properties²⁵.
78 Simorgh et al²⁶ reported a detailed review on additive manufacturing of bioactive glasses via
79 different 3D printing technologies. Lee et al²⁷ reported printing of PEEK via DIW technique using
80 a unique ink. The result shows excellent thermal stability, with a Young's modulus of 2.5 GPa.
81 Despite significant improvements, challenges in bone tissue regeneration remain, including the
82 need for scaffolds resembling natural bone properties.

83 In this study, we propose an innovative approach using a combination of PEEK,
84 carboxymethyl cellulose (CMC), and mesoporous bioactive glass (MBGNs). This proposed study
85 has the potential to overcome existing limitations and offer a practical approach to bone tissue
86 engineering. It provides significant impact on the treatment of bone defects, fractures, and related
87 disorders, ultimately improving the quality life of a patient. Here in, hybrid material manufactured

88 using direct ink write (DIW), aims to overcome limitations by providing precise control over
89 scaffold geometry and pore size. CMC incorporation into the PEEK matrix enhances biological
90 performance, promoting cell attachment, proliferation, and differentiation²⁸. The scaffold is further
91 coated with Zn-Mn doped MBGNs²⁹. The use of MBGNs with PEEK and CMC represents a
92 promising and novel approach to bone tissue engineering. There are limited reported studies for
93 PEEK ink printing by utilizing DIW that promotes bioactivity. It is important to mention that the
94 Zn-Mn MBGNs was not mixed with ink prior to printing. Instead of that Zn-Mn MBGNs was
95 coated on the surface of scaffold which allowed a direct contact between the physiological
96 environment and bioactive particles.

97 The scanning electron microscopy (SEM) is used to study the surface morphology of the
98 scaffold unveils an average pore size of $600 \pm 30 \mu\text{m}$. Furthermore, the coating of bioactive glass
99 is confirmed by energy dispersive x-ray spectroscopy (EDS). Meanwhile, tensile testing confirms
100 the mechanical integrity of the scaffold having a Young's modulus of 2.05 GPa. The antibacterial
101 studies showed that inhibition zones against bacterial strains demonstrate antibacterial behavior
102 and WST-8 cell viability assay shows impressive cell proliferation. The Zn-Mn MBGNs coated
103 PEEK/CMC scaffold is a promising solution for effective osteoporotic treatment, providing a
104 range of features to enhance patient outcomes in the field of bone tissue engineering.

105 **2. Materials and Methods**

106 **2.1. Materials**

107 Commercial polyetheretherketone (PEEK), procured from Germany (704 XF, VictrexTM),
108 serves as the primary material for the scaffold matrix. This thermoplastic exhibit high thermal
109 resistance, chemical resistance, biocompatibility and mechanical properties, respectively.
110 Carboxymethylcellulose (CMC), sourced as carboxymethylcellulose sodium salt from Sigma
111 Aldrich, USA, functions as a supporting material. Its role involves enhancing printability and
112 promoting improved cell adhesion through interactions with glucose transporters facilitated by
113 glucopyranose subunits. Zinc/Manganese-doped mesoporous bioactive glass nanoparticles were
114 synthesized in the laboratory. The chemicals used in the synthesis including
115 hexadecyltrimethylammonium bromide (CTAB) at 98%, zinc nitrate hexahydrate, and tetraethyl
116 orthosilicate (TEOS) at 99%, were sourced from Sigma-Aldrich. Calcium nitrate (Avantor),
117 manganese chloride (Uni-Chem, USA), and ethyl acetate (99.5%, Merck) were utilized.

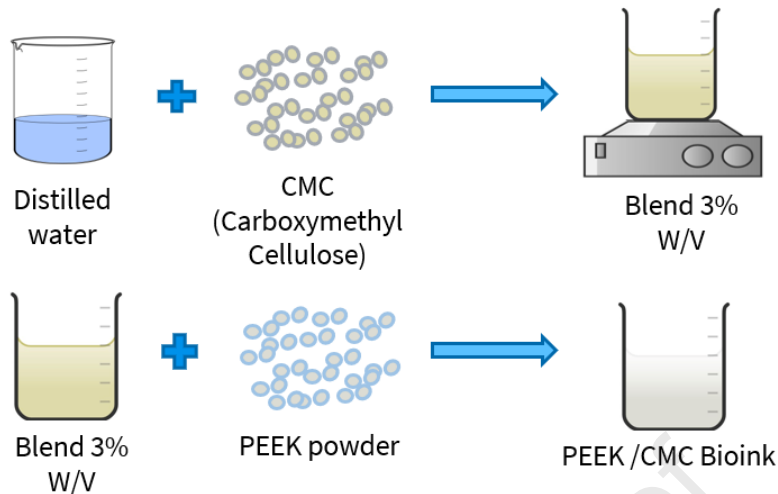
118 **2.2. Synthesis of Mesoporous Bioactive Glass Nanoparticles**

119 Synthesis of Zinc–Manganese-doped mesoporous bioactive glass nanoparticles (Zn-Mn
120 MBGNs) was conducted using the sol-gel method following the Stöber process³⁰. The
121 composition, consisting of SiO₂ (70 mol.%), CaO (22 mol.%), Mn (5 mol.%), and Zn (3 mol.%),
122 was meticulously prepared. The particular composition of Zn-Mn MBGNs was selected on the
123 basis of Batool et al³¹.

124 In brief, a solution consisting of 26 mL distilled water and 0.56 g CTAB was developed
125 following 30 min of stirring at room temperature. Subsequently, 8 mL ethyl acetate and 26 mL
126 ammonium hydroxide (32 vol.%) were introduced, maintaining a pH of 9.5. Then, 6 mL TEOS
127 was added dropwise to the solution. Metal ion precursors, calcium nitrate, and zinc nitrate, were
128 sequentially incorporated under continuous stirring. The solution was left in a dry place for 3 hrs
129 and then subjected to centrifugation at 10,000 rpm for 10 mins to separate the nanoparticles,
130 followed by overnight drying at 70 °C. The final step involved calcination of the nanoparticles in
131 a muffle furnace at 700 °C for 6 hrs.

132 **2.3. Ink synthesis**

133 The initial stage in Direct Ink Write (DIW) involves the synthesis of ink. Small quantities of
134 CMC were dissolved in water until achieving a viscosity suitable for printing³². Usually, PEEK
135 does not dissolve in most biocompatible solvents^{33,34}, it was dispersed in the CMC solution through
136 continuous stirring at 200 rpm and sonicated for 30 mins for a homogeneous suspension. Various
137 ratios of PEEK and CMC were blended using a trial-and-error approach to optimize properties for
138 DIW and tissue engineering. The ultimate composition selected for the maximum amount of PEEK
139 dispersed with the required rheological properties consisted of 3% W/V CMC, with 9.5% W/V
140 PEEK, resulting in the ideal ink for both printing and tissue engineering. Figure 1 shows the
141 schematic processing of Ink synthesis for DIW.



142

143

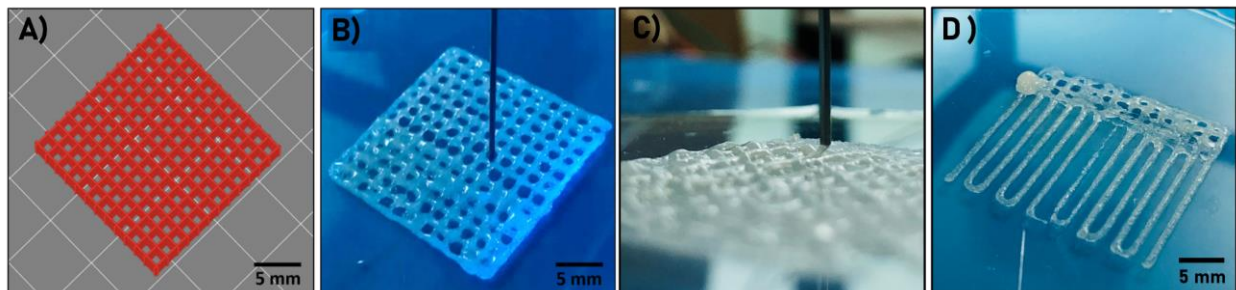
Figure 1. Schematic showing ink synthesis of PEEK/CMC.

144

2.4. Design and fabrication of scaffolds

145 Bone scaffolds required a porosity of up to 85% for effective osteoinduction. Initially, a scaffold
 146 with dimensions 20 mm (L) x 20 mm (W) x 5 mm (H) was designed using SOLIDWORKS 2020
 147 and further refined in Prusaslicer 2.7.1 to generate a Stereolithography (STL) file format. The 3D
 148 print parameters were precisely optimized in alignment with our custom-developed, in-house 3D
 149 printer³⁵. The developed Ink was loaded into a 10 mL syringe, and the scaffold was collected using
 150 a Petri dish, with aluminum serving as the backing plate. Figure 2(A) shows the graphical layout
 151 of the design in the slicing software whereas Figure 2(B) and (C) illustrate a syringe extruder
 152 performing real-time extrusion of PEEK/CMC scaffold according to the design. Whereas Figure
 153 2(D) shows one of the many failures that occurred in the process of optimization of printing
 154 parameters.

155



156 **Figure 2. A) Designing scaffolds, B) C) Real-time 3D printing, and D) Failure during**
 157 **optimization of 3D printing parameters.**

2.5. Crosslinking and Coating

The synthesized scaffolds of PEEK/CMC underwent low crosslinking by adding 3.75% W/W citric acid (CA) to CMC³⁶. This low crosslinking step aimed to maintain the structural integrity of the scaffolds during the coating process³⁷. Afterwards, the scaffolds were dip-coated in a blend of CMC (1 W/V %) and Zn-Mn-doped MBGNs (12 W/V %) under continuous stirring at 300 RPM for 3 min³⁸⁻⁴¹. The CMC adhered to the scaffold surface and polymerized with the CMC already present in the scaffold⁴². Subsequently, the samples underwent another round of crosslinking, but this time a higher crosslinking degree was achieved using 20% W/W CA to CMC³⁶. Prior to crosslinking, all samples were dried at 30 °C for 24 hrs in a vacuum, and the crosslinking reaction took place at 80 °C for 24 hrs³⁶.

2.6. Material Characterization

To assess the rheological properties of the synthesized PEEK/CMC ink, a Brookfield DV-III Viscometer was used. Viscosity spindle (LV-64s) was utilized to characterize the ink by incrementally increasing the shear rate up to 200 s⁻¹. The ink consists of a 3% W/V CMC solution with 7% W/V dispersed PEEK. Rheological analysis serves to define the ink's flowability and yielding characteristics. The resulting flow curve elucidates whether the ink exhibits shear-thinning or shear-thickening behavior, ultimately influencing its printability³⁵.

The morphological study of the 3D fabricated scaffolds was done using a TESCAN (Mira III) field emission scanning electron microscopy (FE-SEM) coupled with an energy dispersive x-ray spectroscopy analyzer (EDS). The pore size and surface porosity of the images were analyzed by ImageJ software.

Attenuated total reflection Fourier transform infrared spectroscope (Thermofisher Nicolet Summit Pro) integrated with OMNIC paradigm software was utilized for the chemical structure analysis. The synthesized scaffold of 10 mg and all the ingredients of the ink were separately used for the FTIR analysis. The background reading was taken against a diamond to eliminate the peaks of noise. The transmittance spectrum was obtained in the range of 4000 cm⁻¹– 400 cm⁻¹ with a resolution of 4 cm⁻¹ by the accumulation of 72 scans.

The mechanical characteristics of the 3D-printed scaffolds were carried out using a Linkam TST350 (UK) tensile testing machine equipped with a 200 N load cell. The scaffolds were 3D printed according to the ASTM D638 *type IV*⁴³ specimen dimensions with a thickness of 3 mm.

188 The test was performed following ASTM D638 standards and the cross-head speed was set at 5
189 mm/min. The testing procedure was conducted in triplicate, and the mean values were
190 subsequently reported.

191 Contact angle measurement is a technique used to evaluate the interfacial surface properties of
192 materials, offering quantitative insights into wettability. In this study, a 50 μ L droplet of distilled
193 water was carefully placed on the scaffold surface using a pipette aid. Images of the scaffolds were
194 then captured at periodic intervals within one min, and were analyzed using the Image JTM
195 software.

196 Swelling is an important factor in defining the drug carrier. To observe the swelling behavior
197 of the fabricated scaffold, three scaffolds were immersed in a phosphate buffer saline (PBS) over
198 the time interval for 1, 5, and 10 days at 37° C. After the specified time period, the scaffolds were
199 weighed to calculate the swelling ratio by using equation (1).

$$200 \quad \text{Swelling Ratio} = \frac{(W_f - W_i)}{W_i} \quad (1)$$

201 The swelling property was measured by equation (1). Initial weight (W_i) and final weight
202 (W_f) were measured before and after immersion in PBS.

203 To investigate the degradation behavior, 30 scaffolds, having an area of 1 x 1 cm², were
204 individually immersed in Falcon tubes containing phosphate-buffered saline (PBS). These tubes
205 were then placed in a shaking incubator set at 37 °C for a duration of 30 days. After 24 hrs, a
206 scaffold was extracted from the solution. The initial and final weights of each scaffold were
207 recorded at every time point, and the weight change was documented for analysis.

208 **2.7. Antibacterial properties**

209 Antibacterial properties of the printed scaffolds were checked against two bacterial strains,
210 Gram-positive, *Staphylococcus aureus* (*S. aureus*) and Gram-negative, *Escherichia coli* (*E. coli*).
211 Square-shaped samples of size 1 cm² were cut and UV-sterilized for 30 mins to be tested against
212 the bacterial strains. Bacterial strains were first cultivated in sterile nutrient broth media for 24 hrs
213 at 37°C with an optical density of 0.015 at 600 nm. An aliquot of 50 μ L strain was uniformly
214 spread on a sterile nutrient agar plate. Control samples without doping of Zn-Mn nanoparticles and
215 test samples (Zn-Mn doped PEEK/CMC scaffolds) were placed on nutrient agar and incubated at

216 37° for 24 hrs. The inhibition zone was measured after 24 hrs to determine the antibacterial efficacy
217 of the scaffolds.

218 **2.8. *In-vivo* chorioallantoic membrane assay**

219 The *in-vivo* chorioallantoic membrane (CAM) assay, a crucial method for evaluating
220 angiogenic potential, was employed to systematically assess the performance of synthesized
221 scaffolds. The fertile Australorp eggs (Day 1) were sourced from the Punjab Poultry Research
222 Institute, cleaned, and incubated under optimal conditions (37 °C, 55–65 % relative humidity) for
223 a further 6 days. The digital egg incubator (HHD 435) was pre-operated for 24 hrs for temperature
224 and humidity equilibrium. Thereafter, eggs were carefully removed, cleaned again with 30 %
225 ethanol, and placed in a biosafety cabinet (Esco class II). A small window (1 × 1 cm²) was created
226 on each eggshell using a sterilized saw blade. The sterilized scaffold sample was then implanted,
227 sealed with sterilized parafilm and adhesive tape, and eggs were returned to the incubator for a 7-
228 day incubation period. On day 14, the eggs were transferred back to the biosafety cabinet, and
229 digital images of developing embryos were captured. Systematic comparison (via ImageJ,
230 Mexican hat filter, color stacking, threshold adjustment, and calculation of branched-chain vessels
231 in the marked zone of interest) with control samples (eggs without scaffolds) facilitated a detailed
232 investigation into the angiogenic potential of the synthesized scaffolds, providing valuable insights
233 into their impact on vascularization within the CAM model.

234 **2.9. Cell culture studies**

235 To perform the WST-8 cell viability assay, human mesenchymal stem cells (MSCs) were
236 selected as the cell model. The scaffolds, precisely sectioned into 1 × 1 cm² pieces, underwent a
237 30 min sterilization process under UV radiation. For cell cultivation, MSCs were nurtured in
238 Dulbecco's Modified Eagle's Medium (DMEM; Gibco) supplemented with 10% fetal bovine
239 serum (FBS; Sigma-Aldrich) and 1% penicillin-streptomycin (Pen Strep; Sigma-Aldrich). The cell
240 cultures were maintained under optimal conditions: 95% relative humidity, 5% CO₂, and a
241 temperature of 37 °C. Each cell test was meticulously executed in triplicate using 10⁵ cells/well in
242 24-well plates.

243 The assessment of cell viability initiated by seeding 10⁵ cells/well with scaffolds, followed
244 by incubation of the cell-scaffold assembly at 37 °C for varying time intervals. At specific time
245 points (1, 3, 5, and 7 days), the WST-8 assay was deployed to gauge cell viability accurately. After

246 discarding the medium, the wells were rinsed twice with PBS. Subsequently, 1 mL of fresh DMEM
247 containing WST-8 (1%) was added to each well, and the mixture was incubated for a designated
248 4 hrs period. The determination of cell viability was quantified by measuring the absorbance at
249 450 nm utilizing a microplate reader, ensuring precise and reproducible results. The similar method
250 was adopted to check the cell viability against bone-forming cells (hFOB 1.19), to investigate the
251 bone regeneration potential of the scaffolds.

252 **2.10. Statistical Analysis**

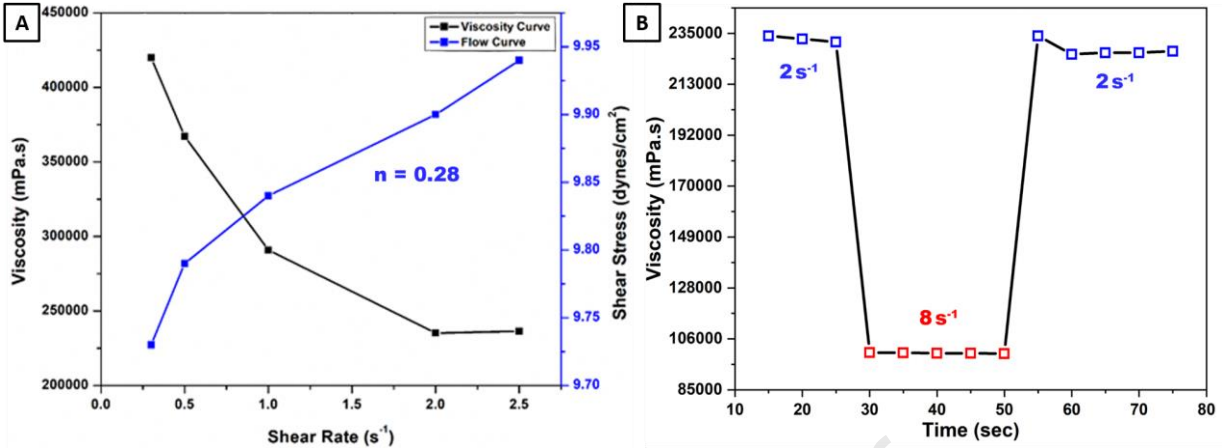
253 The acquired data underwent statistical analysis to assess variations among the various test
254 groups. One-way analysis of variance (ANOVA) was employed, with significance difference (*,
255 $p < 0.05$), followed by Tukey's range test for posthoc analysis. Statistical software, OriginPro 8.5,
256 facilitated the analysis, with reported values presented as mean \pm standard deviation based on
257 triplicate testing.

258 **3. Results and Discussion**

259 **3.1. Rheology and Printability**

260 Among rheological properties viscosity is the most important factor, which affects the
261 extrusion load, motor torque, and decides whether the ink is appropriate for printing. For setting
262 the right speed during printing significant information is gathered about the Ink flow. The Ink must
263 show shear-thinning behavior, which plays a key role in making good print fidelity and keeping
264 its structure intact throughout the printing process⁴⁴. The Ink composition is the main factor during
265 DIW printing that showed the most promising results (in the current study).

266 Figure 3(A) shows the rheological analysis of the Ink and the effect of viscosity and shear
267 stress against shear rate. The flow curves demonstrated a yielding effect around a shear stress of
268 9.77 dyne/cm^2 and at a shear rate of 0.5 s^{-1} . Beyond this point, particles began to arrange
269 themselves in the direction of extrusion. At the shear stress of $\sim 9.85 \text{ dyne/cm}^2$ and at shear rate of
270 $\sim 1 \text{ s}^{-1}$ the ink started to flow from the printer's extruder^{44,45}. Ahmed et al³⁵ also reported similar
271 results for the synthesis of skin scaffolds using DIW



272

273 **Figure 3. (A) Viscosity and Shear Stress analyzed upto a shear rate of 2.5 s⁻¹ (B) Three**
 274 **Interval Thixotropic Test(3ITT), lower shear rate 2 s⁻¹(blue) and upper shear rate 8 s-**
 275 **1(red)**

276 A rapid decline in viscosity with increasing shear rate indicated that the ink possessed a stable,
 277 solid-like structure but behaved like a fluid as the shear rate increased. At the higher shear rates,
 278 the fluid was extruded from the needle and became static once laid onto the bed. This behavior
 279 was analyzed by a three-interval thixotropic test (3ITT)⁴⁶. Figure 3(B) shows that the viscosity
 280 followed its trend after that the shear rate was reduced following an immediate spike. Initially at 2
 281 s⁻¹ in Figure 3(B), the synthesized ink exhibited a viscosity near 230,000 mPa.s. A sudden increase
 282 in shear rate up to 8 s⁻¹ was observed, which indicates the viscosity is reduced to 100,000 mPa.s.
 283 In the final stage, the shear rate was again reduced to the initial rate (2 s⁻¹), and the ink retained its
 284 viscosity within 3 sec. This decrease in viscosity demonstrated excellent shear thinning, beneficial
 285 for extrusion based DIW 3D printing. The ability to retain viscosity within 3 sec indicated good
 286 print fidelity due to high surface tension⁴⁶. According to the power law in equation (2)

287

$$\eta = k \cdot \gamma^{n-1} \quad (2)$$

288 where η is viscosity, k is the consistency factor, γ is shear rate, and n represents the flow
 289 behavior index. Inks with shear-thinning behavior have a value of $n < 1$. By using equation 2, the
 290 flow curve A and the viscosity exponent for the PEEK/CMC ink is 0.28. The printing parameters
 291 illustrated in Table 1 were used to print the scaffolds. Extrusion speed was set at 1.5 mm/s as the
 292 ink flows continuously under a shear stress of 1 s⁻¹ to 2 s⁻¹ (Figure 3 A). In order to achieve a
 293 porosity of 85% the fill density was set as 0.15 and the printing was performed at room
 294 temperature.

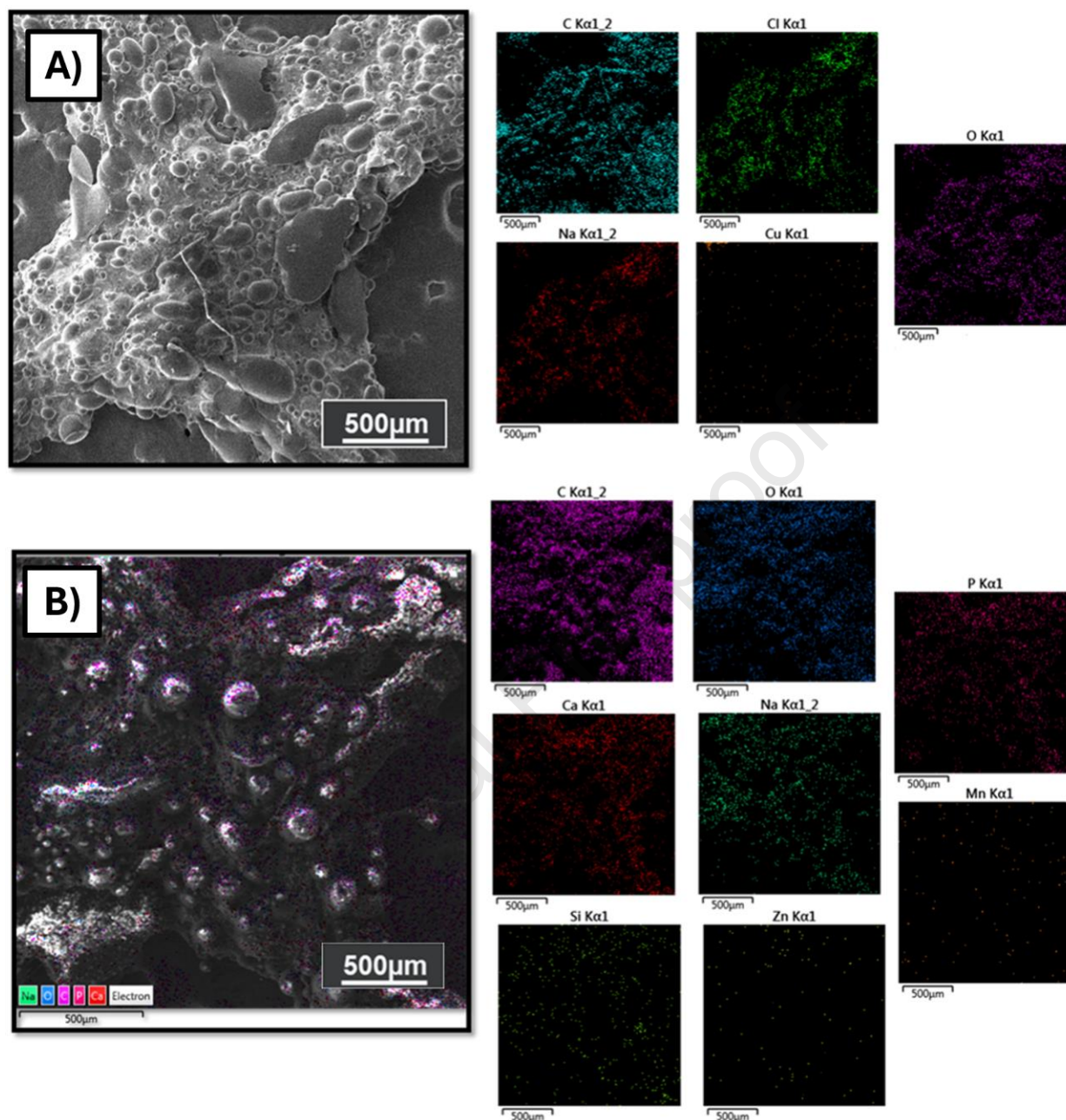
295

Table 1. Parameters for Direct Ink Write 3D Printing

Sr. No.	Parameter	Value
1	Layer Height	0.3mm
2	Extrusion Width	0.3mm
3	Extrusion Speed	1.5 mm/s
4	Nozzle & Bed Temperature	25°C
5	Nozzle Inner Diameter	514 μ m
6	Fill Density	0.15
7	Fill pattern	Rectilinear
8	Fill Angle	45°

296 3.2.Morphological Analysis

297 SEM image at the cross-section of a pristine scaffold is shown in Figure 4(A). The surface
 298 exhibits a high degree of irregularity attributed to the vacuum drying process. However, the
 299 integrity of the scaffold remains intact, underlining its excellent printability and the effectiveness
 300 of the crosslinking process. The layers exhibit remarkable uniformity, and the stability of the ink
 301 is achieved through vigorous stirring. The pore size of the scaffold is quantified by the ImageJ
 302 software. The average pore size was measured as 950 μ m \pm 10 μ m (Figure S1 B supporting
 303 document). After the dip coating process, the scaffold showed strong decrease in pore size to 600
 304 μ m \pm 30 μ m (Figure S1 C supporting document). This alteration in pore size reflects the thickness
 305 of the applied coating. The ideal pore size for osteogenesis and osteoinduction is 500 - 900 μ m⁴⁷.
 306 This pore size encourages transfer of protein and other fluids vital for tissue growth⁴⁷. Moreover,
 307 a larger pore size results in a reduced mechanical strength; this also influences the mechanical
 308 property. Thus, the pore size was engineered to be ~600 μ m.



309

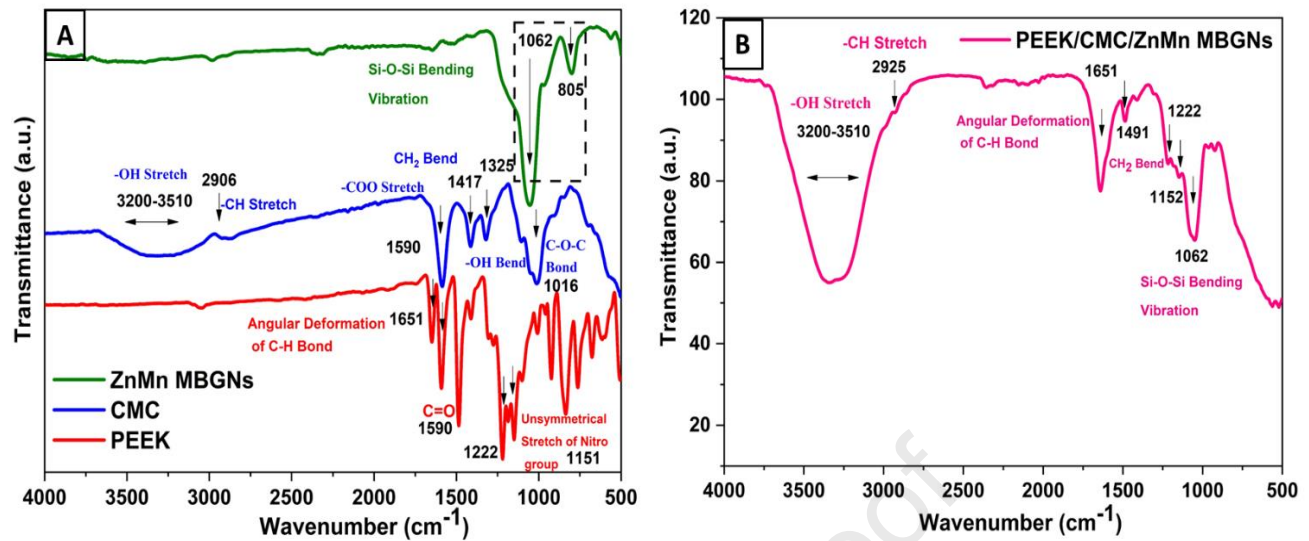
310 **Figure 4. (A) SEM image and EDS mapping of pristine scaffold (B) EDS mapping of coated**
 311 **scaffold showing even distribution of coated elements**

312 Furthermore, EDS mapping was conducted on the coated scaffolds, revealing a uniform
 313 distribution of Si, Zn, and Mn on the surface, as shown in Figure 4(B). Energy dispersive X-ray
 314 spectroscopy (EDS) recorded a weight % of 34.51, 21.64, 31.45, 6.13, 2.13, 1.48, 1.38, 1.28 of C,
 315 Na, O, Si, Ca, P, Mn, Zn respectively. The presence of C, O, and Na is attributed to the PEEK⁴⁸
 316 and CMC; whereas, sodium (Na) salt⁴⁹ was used in ink synthesis. Figure 4B indicates the elemental

317 composition of the deposited Zn-Mn doped mesoporous bioactive glass nanoparticles on the
318 PEEK/CMC scaffold. Figure 4B confirms the presence of Zn and Mn in the PEEK/CMC scaffold
319 after coating. This comprehensive analysis confirms not only the structural robustness of the
320 scaffold but also the successful integration and distribution of the coating components on its
321 surface.

322 **3.3. Fourier Transform Infrared Spectroscopy**

323 FTIR spectra of PEEK, CMC and Zn-Mn MBGNs is shown in Figure 5(A). PEEK showed a
324 peak at 1651 cm^{-1} which is attributed to angular deformation of -CH bond^{50,51}. The symmetrical
325 and unsymmetrical stretching peaks of nitro group appeared at 1222 and 1151 cm^{-1} , respectively⁵⁰.
326 The peak at 1590 cm^{-1} corresponded to carbonyl group^{52,53}. The FTIR analysis of CMC revealed
327 a prominent and wide peak corresponding to the stretching of -OH groups at 3200 to 3510 cm^{-1} ⁵⁴.
328 Additionally, the CMC spectrum exhibited distinct signals at 2906 cm^{-1} attributed to asymmetric
329 stretching of -CH bonds, and at 1590 cm^{-1} indicating asymmetric stretching of -COO ester
330 groups⁵⁵. Subsequently, upon coating of Zn-Mn MBGNs on the scaffold, a reminiscent pattern
331 emerged within the FTIR spectrum, as shown in Figure 5(B) shows the peaks, which correspond
332 to the bending vibration of Si-O-Si bond (805 cm^{-1} and 1062 cm^{-1}) in MBGNs^{31,56}. The FTIR
333 spectra of scaffold showed the broadening of -OH bond from 3200 to 3510 cm^{-1} as shown in
334 Figure 5(B)⁵⁴. The -CH peak at 2925 cm^{-1} in the coated scaffold indicating the presence of CMC⁵⁵.
335 The peaks at 1651 , 1222 and 1152 cm^{-1} , were attributed to angular deformation of -CH bond,
336 symmetric and unsymmetric nitro group of PEEK, respectively^{50,52,53}. However, the peak
337 attributed to Zn-Mn MBGNs appeared at 1062 cm^{-1} (Si-O-Si bending vibrations)³¹. The coating of
338 Zn-Mn MBGNs coated PEEK/CMC scaffold resulted in the shift of various peaks attributed to
339 PEEK, CMC and Zn-Mn MBGNs.



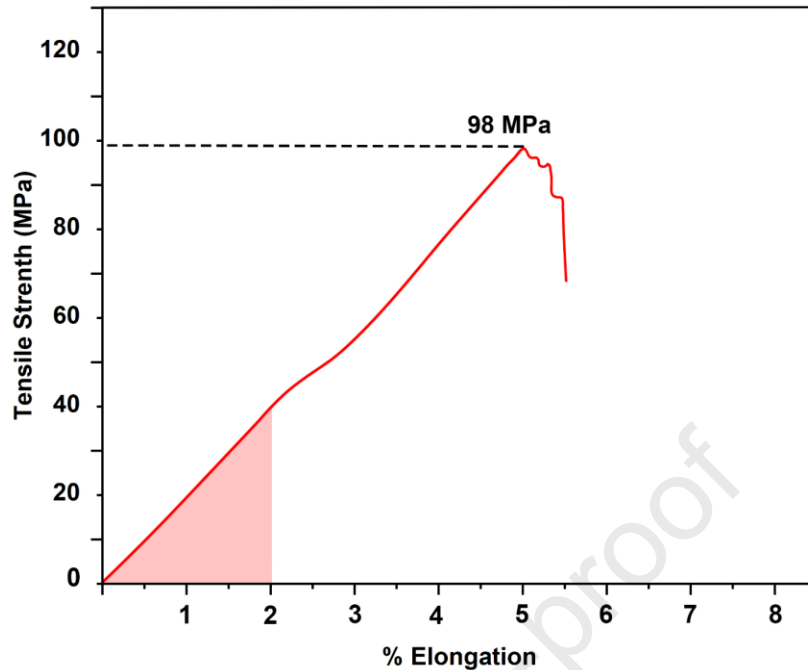
340

341 **Figure 5. FTIR spectra of (A) PEEK, CMC and, Zn-Mn MBGNs (B) PEEK/CMC Zn-Mn**
 342 **MBGNs**

343 3.4. Mechanical Analysis

344 The mechanical response of the PEEK/CMC scaffold under applied tensile forces is depicted
 345 in Figure 6. The tensile test results of the PEEK/CMC 3D printed scaffold unveiled a maximum
 346 tensile strength of 98 MPa and a Young's modulus of 2.05 GPa. The brittle fracture mechanism
 347 observed at the breaking point signifies that the scaffold may experience sudden and abrupt failure
 348 under extreme tensile stress. These findings shed light on the scaffold's capacity to endure tensile
 349 forces until it reaches its breaking point, indicating significant stiffness. The Young's modulus of
 350 commercial PEEK is around 4 GPa⁵⁷, the 3D printed PEEK at room temperature retained 51% of
 351 its Young's modulus. Lee et al, reported a Young's modulus of 2.5 GPa after sintering at 380° C
 352 ²⁷. Comparing the scaffold to an ideal standard for bone tissue engineering, the fabricated 3D
 353 printed scaffold exhibited suitable mechanical properties and are comparable with the previous
 354 studies.⁵⁸⁻⁶⁰. These outcomes imply that the PEEK/CMC scaffold may be optimal for applications
 355 demanding moderate tensile strength, like non-load bearing bone implants. The inherent stiffness
 356 and elasticity of the scaffold as a promising contender for applications in bone tissue engineering
 357 and replacement, where mimicking natural bone's mechanical properties is paramount⁵⁸.

358

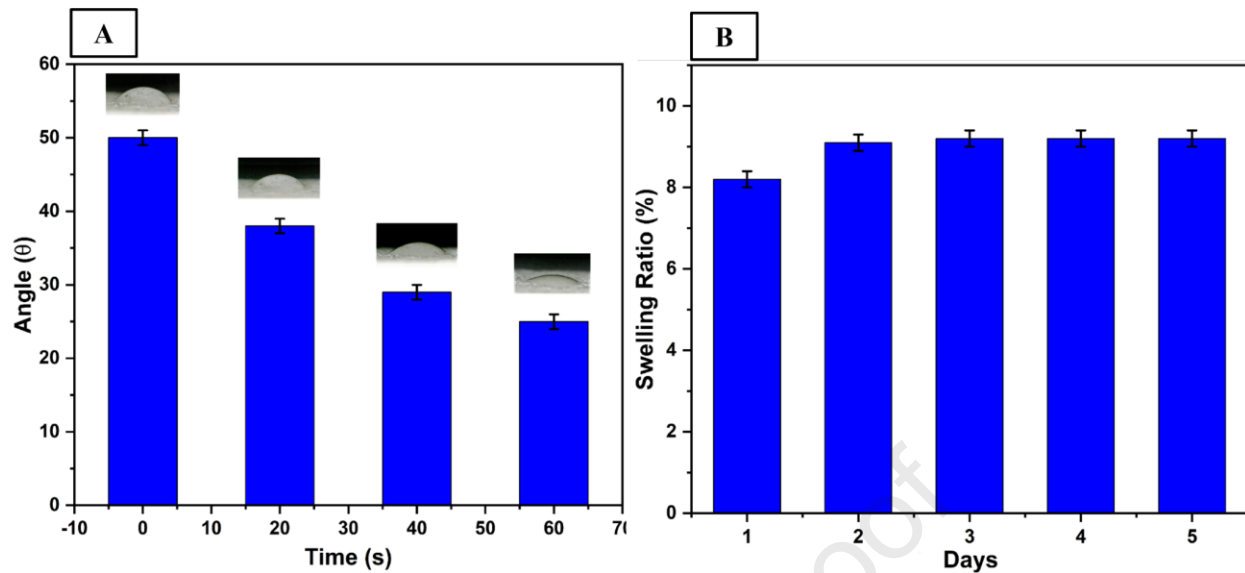


359

360 **Figure 6. Stress strain curve showing the mechanical behavior of scaffold up to the point of**
 361 **fracture**

362 3.5. Wettability studies

363 Wettability is a key factor for bone tissue engineering. Scaffolds that are hydrophilic in nature
 364 can possess bone ingrowth and bone integration⁶¹. Osteoblasts cells generally adhere on the
 365 hydrophilic surfaces which results in cell differentiation. Hydrophilicity of the bone scaffolds
 366 ensures its osteoconductive properties and mimic the bone⁶². A contact angle of 35°–80° is
 367 considered ideal for bone tissue engineering for bone growth⁶³. Singh et al,⁶⁴ reported the
 368 reduction in the contact angle of silk fibroin due to the incorporation of the CMC which enhanced
 369 the cell differentiation. Figure 7(A) shows the reduction in the contact angle of the Zn-Mn
 370 PEEK/CMC scaffold with respect to time. The initial contact angle after dropping the water on the
 371 surface was 50°. The reduction in the contact angle over time confirmed the hydrophilicity of the
 372 scaffold. The hydrophilicity of the scaffold will provide the medium to the osteoblast cells to
 373 adhere onto its surface. The hydrophilic property of the scaffold is attributed to the carboxyl groups
 374 present in CMC to form hydrogen bonds with water molecules⁶⁵. Furthermore, the mesoporous
 375 bioactive glass (MBGNs) provides the essential sites to absorb water on the surface of scaffold.
 376 The results of this study are in agreement with⁶⁵.



377

378 **Figure 7. A) Contact angle measurements of water droplet with respect to time measured on**
 379 **the PEEK/CMC 3D printed scaffold coated with Zn-Mn MBGNs, B) Swelling ratio of**
 380 **scaffold in PBS solution**

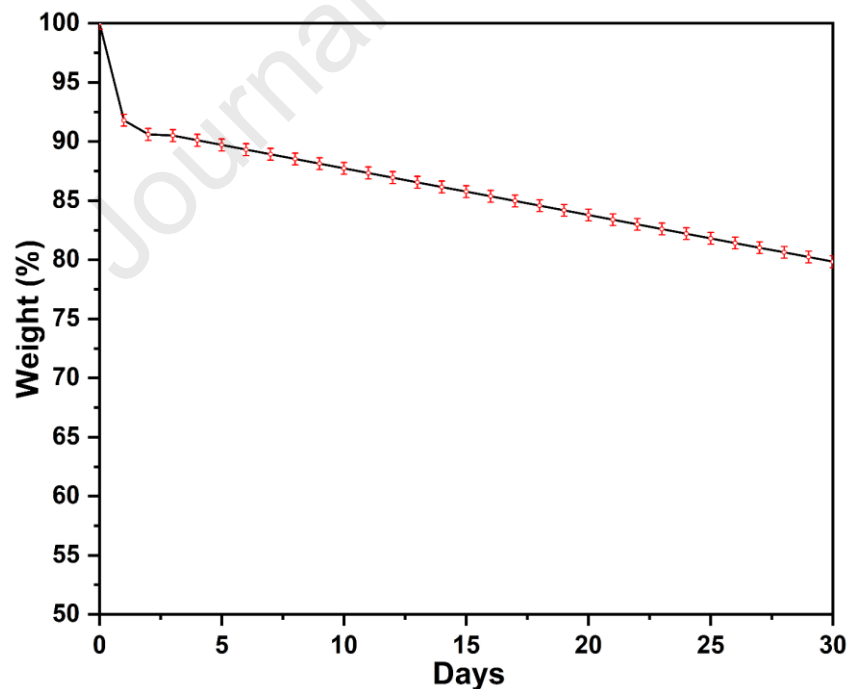
381 3.6.Swelling Studies

382 Swelling ability of the Zn-Mn PEEK/CMC scaffold determines the capability of the scaffold
 383 to swell in the biological fluids. Swelling of the scaffold provides the cells sites to adhere and
 384 differentiate in the biological environment⁶⁶. The controlled swelling of the scaffold leads to the
 385 mechanical stability and osteoconductivity of the scaffold⁶⁷. The excessive swelling in the bone
 386 tissue engineering results in failure and loss in the mechanical integrity of the implants Figure 7(B)
 387 illustrates the swelling ratio of the scaffold. Swelling ratio increased rapidly up to 8 % on 1 day
 388 which confirms the swelling ability of the scaffold. The sustained and controlled swelling ratio
 389 was observed after 2 to 5 days. The increase in the swelling ratio was due to the CMC carboxyl
 390 groups that retain water and form hydrogen bonds when reacting with the biological fluids⁶⁸. The
 391 controlled swelling of the scaffold was due to the PEEK and high degree of citric acid. PEEK is a
 392 hydrophobic material, which cannot adsorb water due to its aromatic rings, ether and ketone
 393 linkages⁶⁹. Furthermore, higher degree of crosslinking resulted in the rigid scaffold, which is less
 394 prone to swelling⁷⁰. The controlled swelling of this study is much similar to the published study⁷¹.

395 3.7.Degradation Studies

396 The degradation study investigated the performance of the Zn-Mn PEEK/CMC scaffold
 397 immersed in phosphate-buffered saline (PBS) for 30 days (Figure 8). After the first 24 hrs, initial

398 observations revealed a substantial degradation of 8%, indicating that the scaffold degrades at a
399 higher rate. This rapid degradation could be attributed to the CMC which is a degradable
400 material⁷². Furthermore, rapid degradation occurs due to the high surface area to volume ratio of
401 CMC^{73,74}. Interestingly, subsequent monitoring demonstrated a consistent degradation rate,
402 resulting in a cumulative degradation of 20% over the 30 days. After 24 hrs, the degradation of the
403 scaffold is reduced in PBS over the time. This could result in a more control and predictable
404 degradation rate⁷⁴. Moreover, mechanical forces also influence the degradation rate. For instance,
405 a higher mechanical force leads to a faster degradation of the scaffolds⁷⁵. The inherent properties
406 of PEEK, known for its high resistance to chemical and thermal degradation controlled the
407 degradation rate during immersion in PBS⁷⁶. The rapid initial degradation observed in the first day
408 suggests a dynamic response of the scaffold to the environmental conditions and is better for the
409 initial release of drug required in the first 24 hrs of installation. As the study progressed, the
410 sustained degradation implies gradual regeneration for bone tissue⁷⁷. Moreover, the coated
411 MBGNs on the scaffold and its degradation influence the osteogenesis and tissue regeneration
412 processes⁷⁶.

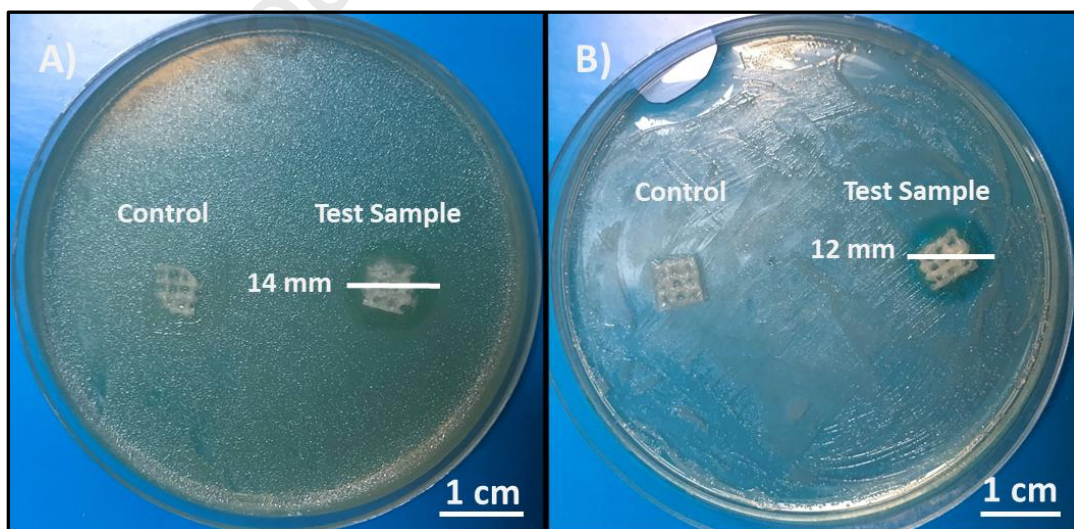


413

414 **Figure 8. Degradation studies showing loss in percentage weight of the Zn-Mn PEEK/CMC**
415 **Scaffold over 30 days**

416 3.8. Antibacterial Study

417 PEEK is considered as a bioinert material, and its biomedical applications are limited. In the
418 present study, zinc nanoparticles have been doped in PEEK/CMC scaffold in order to enhance its
419 effectiveness against two types of bacteria, Gram positive, *Staphylococcus aureus* (*S. aureus*) and
420 Gram negative, *Escherichia coli* (*E. coli*). The results of disk diffusion test showed an excellent
421 antibacterial efficacy against *S. aureus* with inhibition zone of 14 mm and inhibition zone of 12
422 mm was measured against *E. coli* shown in Figure 9(A and B). This result may be interpreted by
423 the ability of zinc nanoparticles to effect on both gram positive and gram negative, but it showed
424 high efficacy against gram positive as compared to gram negative bacteria. This belongs to the
425 difference in their cell wall structure as gram negative bacteria have an additional outer membrane
426 which acts as a barrier against many antibacterial agents to penetrate the cell wall⁷⁸. The inhibition
427 of bacterial growth is attributed to the ability of zinc nanoparticles which interact with bacterial
428 cell membrane and disrupt the integrity of bacterial structure leading to the release of cellular
429 components hence analysis of the whole bacterial cell. Zinc nanoparticles can also create reactive
430 oxygen species which interact with bacterial cells, lead to oxidative damage to cellular
431 components of bacteria (DNA, proteins and lipids), ultimately, causes cell death^{79,80}. Based on the
432 above, Zn-Mn PEEK/CMC scaffolds have an excellent antibacterial efficacy and can potentially
433 be used in biomedical applications.



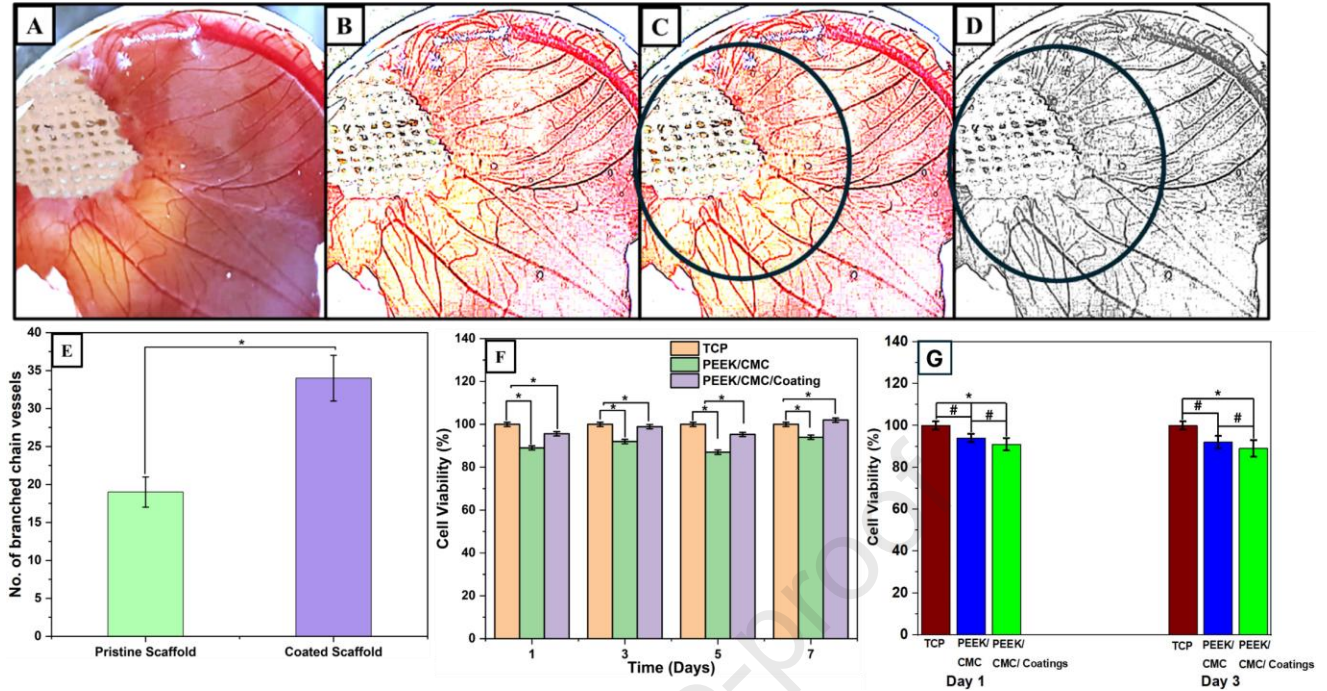
434

435 **Figure 9. Antibacterial activity of PEEK/CMC scaffold (control) and Zn-Mn doped**
436 **PEEK/CMC scaffold (test sample) against (A) Gram positive, *S. aureus* and (B) Gram**
437 **negative, *E. coli***

438 3.9.CAM Assay

439 The results of the CAM assay for the PEEK/CMC scaffold coated with Zn/Mn doped MBGNs
440 showed a significant increase in several branched-chain vessels in comparison to eggs with the
441 pristine scaffold (as shown in Figure 10(E)). This suggests a strong angiogenic response, which is
442 crucial for tissue regeneration. Angiogenesis is the formation of new capillaries from existing
443 blood vessels⁸¹, and is a complex process influenced by various factors. In the PEEK/CMC
444 scaffold, CMC has been shown to have pro-angiogenic effects. Studies have found that CMC-
445 derived extracellular vessels can enhance cell migration, tube formation, and survival under
446 peroxide exposure, which are key steps in angiogenesis⁸².

447 Manganese (Mn) ions also play a role in angiogenesis. Mn ions can regulate exosome
448 production and function, affecting immune response, angiogenesis, and osteogenesis⁷⁸. The
449 number of branched chain blood vessels in the CAM assay was calculated by using the plugin
450 Mexican hat filter of ImageJ and marking the zone of interest around the sample. Followed by
451 counting the number of branched chain vessels in the marked zone of interest (as shown in Figure
452 10(A-D)). This provided a quantitative measure of branched-chain vessels both in control (pristine
453 scaffold) and Zn/Mn doped MBGNs coated scaffold. This makes PEEK/CMC scaffold a promising
454 material for applications that require enhanced tissue regeneration.



455

456 **Figure 10. (A-D) Coated scaffold on fertile Australorp eggs after 14 days of incubation, (A)**
 457 **optical image, (B) image after applying the Mexican Hat Filter, (C) after adjusting threshold**
 458 **and marking area of interest, (D) after conversion to 8-bit, (E) No. of branched chain vessels**
 459 **in pristine scaffold and Zn/Mn doped MBGNs coated scaffold, (F) WST-8 assay for pristine**
 460 **and coated scaffolds against MSCs, and (G) WST-8 assay for pristine and coated scaffolds**
 461 **against bone forming cells (osteoblasts) (one-way ANNOVA was applied and * represent the**
 462 **significant difference)**

463 3.10. Cell Culture

464 As shown in Figure 10(F), the cell viability for PEEK/CMC pristine recorded at day 1, 3, 5,
 465 and 7 was 85%, 87%, 83% and 91%, and 97%, 98%, 96% and 103% for coated scaffold
 466 respectively. Scaffolds should possess interconnected porous structure and high porosity to be used
 467 in the field of tissue engineering. The porosity provides a site for cell attachment, proliferation and
 468 supports the migration of nutrients and gases for cells nourishment⁸³. As observed from
 469 morphological analysis from Figure 4, the scaffold exhibited a porous and irregular surface which
 470 can be attributed to the addition of CMC. CMC promotes initial cell attachment due to the presence
 471 of functional groups which are hydrophilic in nature⁴⁹. Cell adhesion is a necessary step which
 472 further facilitates mesenchymal cells differentiation and proliferation. The biocompatible nature
 473 of CMC makes it a suitable candidate for tissue engineering applications as it creates biomimetic
 474 environment for MSCs for their survival and function.

475 Similarly, both the pristine PEEK/CMC and PEEK/CMC coating were cytocompatible
476 against bone-forming osteoblast cells, as shown in Figure 10G. The porous nature of the developed
477 scaffold supposedly aided in the attachment and proliferation of osteoblast cells⁸⁴. Moreover, the
478 hydrophilic nature of scaffolds may also contribute to enhanced cellular attachment⁸⁵.
479 Furthermore, the incorporation of Mn in MBGNS might upregulate the cell proliferation. The
480 release of Mn ions in biological fluids may influence osteoblast cell behavior, as it acts as a
481 cofactor for enzyme activation and also aids in cross-linking of collagen fibers⁸⁶. Mn is involved
482 in the activation of signaling molecules and transcription factors such as Runt-related transcription
483 factor 2 (RUNX 2) and Bone morphogenetic proteins (BMPs)⁸⁷. The possible release of Mn ions
484 modulates these molecules which promote osteoblast cell proliferation. Doping of Mn in MBGNS
485 improved its biological properties. The PEEK/CMC pristine and coated scaffolds prepared in the
486 present study exhibited remarkable cell viability. Hence, the prepared scaffold in the present study
487 is a suitable candidate for bone tissue engineering applications.

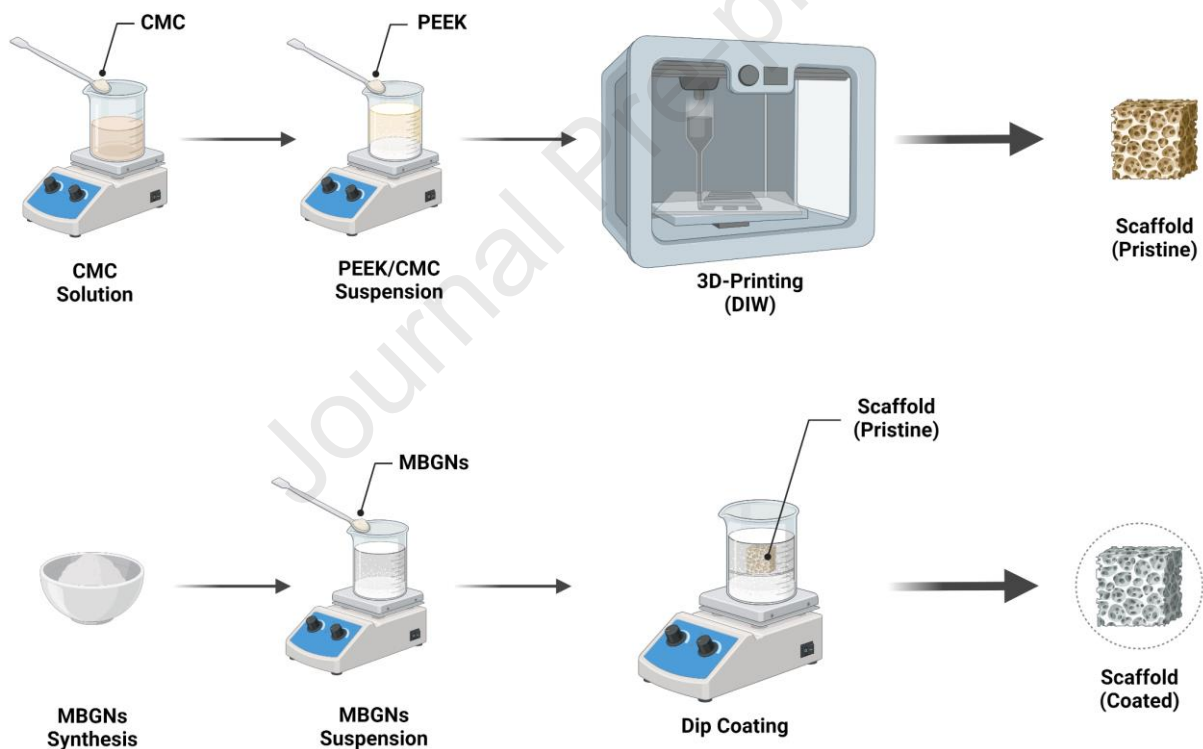
488 **Conclusions**

489 Our investigation into the fabrication of a patient-specific scaffold for the rapid recovery from
490 osteoporotic fractures represent a significant advancement in the field of biomaterial-based
491 implants. The developed ink is a blend of PEEK and CMC coated Zn-Mn doped MBGNS, not only
492 shows impressive shear-thinning behavior but also offers enhanced printability which is favorable
493 for scaffold fabrication. The application of Direct Ink Write (DIW) 3D-printing techniques results
494 in bone scaffold fabrication by using parameters: 85% porosity, 0.3 mm layer height, and a printing
495 speed of 1.5 mm/s. The subsequent deposition of Zn-Mn MBGNS on the fabricated scaffolds using
496 a dip-coating method serves to augment osteoinductive and bone regenerative properties, as
497 confirmed by scanning electron microscopy (SEM) with an average pore size of $600 \pm 30 \mu\text{m}$.
498 EDS results showed an excellent bioactive glass coating on the scaffold.

499 FTIR results validate the presence of PEEK, CMC, and Zn-Mn MBGNS functional groups in
500 the scaffold, signifying the successful incorporation of the bioactive glass coating, which is good
501 in agreement with EDS results. Tensile testing reveals Young's modulus of 2.05 GPa, affirming
502 the mechanical properties of scaffold for specific load-bearing applications. The antibacterial halo
503 tests demonstrate a notable inhibition zone against both *Staphylococcus aureus* and *Escherichia*
504 *Coli* strains, emphasizing the scaffold's potential for infection control. CAM assays reveal an

505 increased angiogenic response, attributed to the bioactive glass coating, highlighting angiogenic
 506 potential of the scaffold in promoting tissue regeneration. Additionally, WST-8 cell viability
 507 assays demonstrate impressive cell proliferation due to presence of porosity, CMC, and Mn ions,
 508 with a remarkable 103% viability at day 7, defining the biocompatibility and bioactivity of the
 509 scaffold. This comprehensive investigation amalgamates advanced engineering techniques with
 510 novel biomaterials, presenting the Zn-Mn PEEK/CMC scaffold as a promising and tailored
 511 solution for the treatment of osteoporotic fractures. The study shows that the scaffold is used in
 512 bone tissue engineering, providing a customized and effective approach for faster recovery and
 513 better patient results.

514 ToC Graphics



517 References

- 518 1. Prasad, K. *et al.* Metallic Biomaterials: Current Challenges and Opportunities. *Materials*
 519 (*Basel*). **10**, (2017).
- 520 2. Chen, Q. & Thouas, G. A. Metallic implant biomaterials. *Mater. Sci. Eng. R Reports* **87**, 1–

- 521 57 (2015).
- 522 3. Dapunt, U. *et al.* On the inflammatory response in metal-on-metal implants. *J. Transl. Med.*
523 **12**, 74 (2014).
- 524 4. Biswal, T. Biopolymers for tissue engineering applications: A review. *Mater. Today Proc.*
525 **41**, 397–402 (2021).
- 526 5. Asl, M. A., Karbasi, S., Beigi-Boroujeni, S., Zamanlui Benisi, S. & Saeed, M. Evaluation
527 of the effects of starch on polyhydroxybutyrate electrospun scaffolds for bone tissue
528 engineering applications. *Int. J. Biol. Macromol.* **191**, 500–513 (2021).
- 529 6. Navarro, M., Michiardi, A., Castano, O. & Planell, J. A. Biomaterials in orthopaedics. *J. R.*
530 *Soc. interface* **5**, 1137–1158 (2008).
- 531 7. Rae, P. J., Brown, E. N. & Orler, E. B. The mechanical properties of poly(ether-ether-
532 ketone) (PEEK) with emphasis on the large compressive strain response. *Polymer (Guildf).*
533 **48**, 598–615 (2007).
- 534 8. Zheng, J. *et al.* Additively-manufactured PEEK/HA porous scaffolds with excellent
535 osteogenesis for bone tissue repairing. *Compos. Part B Eng.* **232**, 109508 (2022).
- 536 9. Gu, X. *et al.* Bioinspired modifications of PEEK implants for bone tissue engineering.
537 *Front. Bioeng. Biotechnol.* **8**, 631616 (2021).
- 538 10. Liao, C., Li, Y. & Tjong, S. C. Polyetheretherketone and its composites for bone
539 replacement and regeneration. *Polymers (Basel)*. **12**, 2858 (2020).
- 540 11. Dondani, J. R., Iyer, J. & Tran, S. D. Surface Treatments of PEEK for Osseointegration to
541 Bone. *Biomolecules* **13**, 464 (2023).
- 542 12. Xie, W., Yang, Z., Zhou, Y., Xu, X. & Hu, K. Research Progress of 3D Bioprinting PEEK
543 Scaffold Material for Bone Regeneration. in *China Academic Conference on Printing and*
544 *Packaging* 136–144 (Springer, 2023).
- 545 13. Ma, R. & Tang, T. Current strategies to improve the bioactivity of PEEK. *Int. J. Mol. Sci.*
546 **15**, 5426–5445 (2014).
- 547 14. Panayotov, I. V., Orti, V., Cuisinier, F. & Yachouh, J. Polyetheretherketone (PEEK) for
548 medical applications. *J. Mater. Sci. Mater. Med.* **27**, 1–11 (2016).
- 549 15. Wilt, J. K., Gilmer, D., Kim, S., Compton, B. G. & Saito, T. Direct ink writing techniques
550 for in situ gelation and solidification. *MRS Commun.* **11**, 106–121 (2021).
- 551 16. Somers, N. *et al.* Fabrication of doped β -tricalcium phosphate bioceramics by Direct Ink
552 Writing for bone repair applications. *J. Eur. Ceram. Soc.* **43**, 629–638 (2023).
- 553 17. Sahakyants, T. & Vacanti, J. P. Tissue engineering: From the bedside to the bench and back
554 to the bedside. *Pediatr. Surg. Int.* **36**, 1123–1133 (2020).
- 555 18. Highley, C. B., Song, K. H., Daly, A. C. & Burdick, J. A. Jammed microgel inks for 3D
556 printing applications. *Adv. Sci.* **6**, 1801076 (2019).
- 557 19. Dong, D. *et al.* Enhanced mechanical properties and biological responses of SLA 3D printed

- 558 biphasic calcium phosphate bioceramics by doping bioactive metal elements. *J. Eur. Ceram.*
559 *Soc.* **43**, 4167–4178 (2023).
- 560 20. Abdelaziz, A. G. *et al.* A Review of 3D Polymeric Scaffolds for Bone Tissue Engineering:
561 Principles, Fabrication Techniques, Immunomodulatory Roles, and Challenges.
562 *Bioengineering* **10**, 204 (2023).
- 563 21. Roseti, L. *et al.* Scaffolds for bone tissue engineering: state of the art and new perspectives.
564 *Mater. Sci. Eng. C* **78**, 1246–1262 (2017).
- 565 22. Bose, S., Koski, C. & Vu, A. A. Additive manufacturing of natural biopolymers and
566 composites for bone tissue engineering. *Mater. Horizons* **7**, 2011–2027 (2020).
- 567 23. Wang, C. *et al.* 3D printing of bone tissue engineering scaffolds. *Bioact. Mater.* **5**, 82–91
568 (2020).
- 569 24. Madrid, A. P. M., Vrech, S. M., Sanchez, M. A. & Rodriguez, A. P. Advances in additive
570 manufacturing for bone tissue engineering scaffolds. *Mater. Sci. Eng. C* **100**, 631–644
571 (2019).
- 572 25. Peng, S. *et al.* Graphene oxide as an interface phase between polyetheretherketone and
573 hydroxyapatite for tissue engineering scaffolds. *Sci. Rep.* **7**, 46604 (2017).
- 574 26. Simorgh, S. *et al.* Additive manufacturing of bioactive glass biomaterials. *Methods* **208**,
575 75–91 (2022).
- 576 27. Lee, C.-U. *et al.* Room temperature extrusion 3D printing of polyether ether ketone using a
577 stimuli-responsive binder. *Addit. Manuf.* **28**, 430–438 (2019).
- 578 28. Agis, H., Beirer, B., Watzek, G. & Gruber, R. Effects of carboxymethylcellulose and
579 hydroxypropylmethylcellulose on the differentiation and activity of osteoclasts and
580 osteoblasts. *J. Biomed. Mater. Res. Part A* **95**, 504–509 (2010).
- 581 29. Westhauser, F. *et al.* Effect of manganese, zinc, and copper on the biological and osteogenic
582 properties of mesoporous bioactive glass nanoparticles. *J. Biomed. Mater. Res. Part A* **109**,
583 1457–1467 (2021).
- 584 30. Li, W. & Zhao, D. Extension of the Stöber method to construct mesoporous SiO₂ and TiO₂
585 shells for uniform multifunctional core–shell structures. *at* (2013).
- 586 31. Batool, S. A., Ahmad, K., Irfan, M. & Ur Rehman, M. A. Zn–Mn-doped mesoporous
587 bioactive glass nanoparticle-loaded zein coatings for bioactive and antibacterial orthopedic
588 implants. *J. Funct. Biomater.* **13**, 97 (2022).
- 589 32. Li, X., Zhang, P., Li, Q., Wang, H. & Yang, C. Direct-ink-write printing of hydrogels using
590 dilute inks. *IScience* **24**, (2021).
- 591 33. da Silva Burgal, J., Peeva, L. G., Kumbharkar, S. & Livingston, A. Organic solvent resistant
592 poly (ether-ether-ketone) nanofiltration membranes. *J. Memb. Sci.* **479**, 105–116 (2015).
- 593 34. Trotta, F., Drioli, E., Moraglio, G. & Poma, E. B. Sulfonation of polyetheretherketone by
594 chlorosulfuric acid. *J. Appl. Polym. Sci.* **70**, 477–482 (1998).

- 595 35. Ahmed, S. *et al.* 3D Printing Assisted Fabrication of Copper-Silver Mesoporous Bioactive
596 Glass Nanoparticles Reinforced Sodium Alginate/Poly(vinyl alcohol) Based Composite
597 Scaffolds: Designed for Skin Tissue Engineering. *ACS Appl. Bio Mater.* **6**, 5052–5066
598 (2023).
- 599 36. Demitri, C. *et al.* Novel superabsorbent cellulose-based hydrogels crosslinked with citric
600 acid. *J. Appl. Polym. Sci.* **110**, 2453–2460 (2008).
- 601 37. Raucci, M. G. *et al.* Effect of citric acid crosslinking cellulose-based hydrogels on
602 osteogenic differentiation. *J. Biomed. Mater. Res. Part A* **103**, 2045–2056 (2015).
- 603 38. Qian, Y. *et al.* Protonation and dip-coating synergistically enhancing dimensional stability
604 of multifunctional cellulose-based films. *Cellulose* **29**, 967–983 (2022).
- 605 39. Tran, D.-T., Chen, F.-H., Wu, G.-L., Ching, P. C. O. & Yeh, M.-L. Influence of Spin
606 Coating and Dip Coating with Gelatin/Hydroxyapatite for Bioresorbable Mg Alloy
607 Orthopedic Implants: In Vitro and In Vivo Studies. *ACS Biomater. Sci. Eng.* **9**, 705–718
608 (2023).
- 609 40. Falamaki, C., Naimi, M. & Aghaie, A. Dip-coating technique for the manufacture of
610 alumina microfilters using PVA and Na-CMC as binders: a comparative study. *J. Eur.*
611 *Ceram. Soc.* **26**, 949–956 (2006).
- 612 41. Baligheid, S. M., Arunkumar, T., Thodda, G. & Elangovan, K. Fabrication of HAp/rGO
613 nanocomposite coating on PEEK: Tribological performance study. *Surfaces and Interfaces*
614 **38**, 102865 (2023).
- 615 42. Guo, H., Hamielec, A. E. & Zhu, S. Experimental study of emulsion polymerization with
616 crosslinking. *J. Appl. Polym. Sci.* **66**, 935–957 (1997).
- 617 43. Raj, S. S., Kuzmin, A. M., Subramanian, K., Sathiamoorthy, S. & Kandasamy, K. T.
618 Philosophy of selecting ASTM standards for mechanical characterization of polymers and
619 polymer composites. *Mater. Plast.* **58**, 247–256 (2021).
- 620 44. Saadi, M. *et al.* Direct ink writing: a 3D printing technology for diverse materials. *Adv.*
621 *Mater.* **34**, 2108855 (2022).
- 622 45. Wei, P. *et al.* Go with the flow: Rheological requirements for direct ink write printability.
623 *J. Appl. Phys.* **134**, (2023).
- 624 46. del-Mazo-Barbara, L. & Ginebra, M.-P. Rheological characterisation of ceramic inks for
625 3D direct ink writing: A review. *J. Eur. Ceram. Soc.* **41**, 18–33 (2021).
- 626 47. Ran, Q. *et al.* Osteogenesis of 3D printed porous Ti6Al4V implants with different pore
627 sizes. *J. Mech. Behav. Biomed. Mater.* **84**, 1–11 (2018).
- 628 48. Bhatnagar, N., Jha, S. & Bhowmik, S. Energy dispersive spectroscopy study of surface
629 modified PEEK. *Adv. Mater. Lett.* **2**, 52–57 (2012).
- 630 49. Kurdtabar, M., Nezam, H., Rezanejade Bardajee, G., Dezfulian, M. & Salimi, H.
631 Biocompatible magnetic hydrogel nanocomposite based on carboxymethylcellulose:
632 synthesis, cell culture property and drug delivery. *Polym. Sci. Ser. B* **60**, 231–242 (2018).

- 633 50. Rehman, M. A. U., Bastan, F. E., Haider, B. & Boccaccini, A. R. Electrophoretic deposition
634 of PEEK/bioactive glass composite coatings for orthopedic implants: A design of
635 experiments (DoE) study. *Mater. Des.* **130**, 223–230 (2017).
- 636 51. Nawaz, A., Bano, S., Yasir, M., Wadood, A. & Rehman, M. A. U. Ag and Mn-doped
637 mesoporous bioactive glass nanoparticles incorporated into the chitosan/gelatin coatings
638 deposited on PEEK/bioactive glass layers for favorable osteogenic differentiation and
639 antibacterial activity. *Mater. Adv.* **1**, 1273–1284 (2020).
- 640 52. Rehman, M. M., Shaker, K. & Nawab, Y. Effect of PEEK particles on biomechanical
641 behavior of carbon/epoxy composite. *Int. J. Polym. Sci.* **2022**, (2022).
- 642 53. Zhou, H., Goel, V. K. & Bhaduri, S. B. A fast route to modify biopolymer surface: a study
643 on polyetheretherketone (PEEK). *Mater. Lett.* **125**, 96–98 (2014).
- 644 54. Rani, M. S. A., Rudhzhiah, S., Ahmad, A. & Mohamed, N. S. Biopolymer electrolyte based
645 on derivatives of cellulose from kenaf bast fiber. *Polymers (Basel)*. **6**, 2371–2385 (2014).
- 646 55. Kumar, B. *et al.* Nanoporous sodium carboxymethyl cellulose-g-poly (Sodium
647 acrylate)/FeCl₃ hydrogel beads: Synthesis and characterization. *Gels* **6**, 49 (2020).
- 648 56. Ahmad, K. *et al.* Electrophoretic deposition, microstructure and selected properties of
649 zein/cloves coatings on 316L stainless steel. *Prog. Org. Coatings* **176**, 107407 (2023).
- 650 57. Sandler, J. *et al.* Carbon-nanofibre-reinforced poly(ether ether ketone) composites. *Compos.*
651 *Part A Appl. Sci. Manuf.* **33**, 1033–1039 (2002).
- 652 58. Velasco, M. A., Narváez-Tovar, C. A. & Garzón-Alvarado, D. A. Design, materials, and
653 mechanobiology of biodegradable scaffolds for bone tissue engineering. *Biomed Res. Int.*
654 **2015**, (2015).
- 655 59. Chao, L. *et al.* Analysis of mechanical properties and permeability of trabecular-like porous
656 scaffold by additive manufacturing. *Front. Bioeng. Biotechnol.* **9**, 779854 (2021).
- 657 60. Zeng, S., He, W., Wang, J., Xu, M. & Wei, T. Structural Design and Mechanical Properties
658 Analysis of Fused Triply Periodic Minimal Surface Porous Scaffold. *J. Mater. Eng.*
659 *Perform.* **32**, 4083–4096 (2023).
- 660 61. Boyan, B. D., Lotz, E. M. & Schwartz, Z. Roughness and Hydrophilicity as Osteogenic
661 Biomimetic Surface Properties. *Tissue Eng. Part A* **23**, 1479–1489 (2017).
- 662 62. Kazimierczak, P. & Przekora, A. Osteoconductive and osteoinductive surface modifications
663 of biomaterials for bone regeneration: A concise review. *Coatings* **10**, 971 (2020).
- 664 63. Bil, M., Ryszkowska, J., Woźniak, P., Kurzydłowski, K. J. & Lewandowska-Szumieł, M.
665 Optimization of the structure of polyurethanes for bone tissue engineering applications.
666 *Acta Biomater.* **6**, 2501–2510 (2010).
- 667 64. Singh, B. N., Panda, N. N., Mund, R. & Pramanik, K. Carboxymethyl cellulose enables silk
668 fibroin nanofibrous scaffold with enhanced biomimetic potential for bone tissue engineering
669 application. *Carbohydr. Polym.* **151**, 335–347 (2016).
- 670 65. Rahman, M. S. *et al.* Recent developments of carboxymethyl cellulose. *Polymers (Basel)*.

- 671 **13**, 1345 (2021).
- 672 66. Matyash, M., Despang, F., Ikonomidou, C. & Gelinsky, M. Swelling and mechanical
673 properties of alginate hydrogels with respect to promotion of neural growth. *Tissue Eng.*
674 *Part C Methods* **20**, 401–411 (2014).
- 675 67. Mendonca, R. H., de Oliveira Meiga, T., da Costa, M. F. & da Silva Moreira Thire, R. M.
676 Production of 3D scaffolds applied to tissue engineering using chitosan swelling as a
677 porogenic agent. *J. Appl. Polym. Sci.* **129**, 614–625 (2013).
- 678 68. Dogigli, M., Handrick, K., Bickel, M. & Fröhlich, A. CMC key technologies-background,
679 status, present and future applications. in *Hot Structures and Thermal Protection Systems*
680 *for Space Vehicles* vol. 521 79 (2003).
- 681 69. Ourahmoune, R., Salvia, M., Mathia, T. G. & Mesrati, N. Surface morphology and
682 wettability of sandblasted PEEK and its composites. *Scanning J. Scanning Microsc.* **36**, 64–
683 75 (2014).
- 684 70. Wu, H. *et al.* Effect of citric acid induced crosslinking on the structure and properties of
685 potato starch/chitosan composite films. *Food Hydrocoll.* **97**, 105208 (2019).
- 686 71. Hasan, A., Waibhaw, G., Saxena, V. & Pandey, L. M. Nano-biocomposite scaffolds of
687 chitosan, carboxymethyl cellulose and silver nanoparticle modified cellulose nanowhiskers
688 for bone tissue engineering applications. *Int. J. Biol. Macromol.* **111**, 923–934 (2018).
- 689 72. Weng, L., Rostamzadeh, P., Nooryshokry, N., Le, H. C. & Golzarian, J. In vitro and in vivo
690 evaluation of biodegradable embolic microspheres with tunable anticancer drug release.
691 *Acta Biomater.* **9**, 6823–6833 (2013).
- 692 73. Oladapo, B., Zahedi, A., Ismail, S., Fernando, W. & Ikumapayi, O. 3D-printed biomimetic
693 bone implant polymeric composite scaffolds. *Int. J. Adv. Manuf. Technol.* 1–9 (2023).
- 694 74. Oladapo, B. I. *et al.* 3D printing of PEEK–cHAp scaffold for medical bone implant. *Bio-*
695 *Design Manuf.* **4**, 44–59 (2021).
- 696 75. Gummadi, S. K., Saini, A., Owusu-Danquah, J. S. & Sikder, P. Mechanical properties of
697 3D-printed porous poly-ether-ether-ketone (PEEK) orthopedic scaffolds. *JOM* **74**, 3379–
698 3391 (2022).
- 699 76. Zohoor, S., Abolfathi, N. & Solati-Hashjin, M. Accelerated degradation mechanism and
700 mechanical behavior of 3D-printed PLA scaffolds for bone regeneration. *Iran. Polym. J.* **32**,
701 1209–1227 (2023).
- 702 77. Kacvinská, K. *et al.* Porous cellulose-collagen scaffolds for soft tissue regeneration:
703 influence of cellulose derivatives on mechanical properties and compatibility with adipose-
704 derived stem cells. *Cellulose* **29**, 8329–8351 (2022).
- 705 78. Bannerman, D. D. *et al.* Escherichia coli and Staphylococcus aureus elicit differential innate
706 immune responses following intramammary infection. *Clin. Vaccine Immunol.* **11**, 463–472
707 (2004).
- 708 79. Reyes-Vidal, Y. *et al.* Electrodeposition, characterization, and antibacterial activity of

- 709 zinc/silver particle composite coatings. *Appl. Surf. Sci.* **342**, 34–41 (2015).
- 710 80. Mendes, C. R. *et al.* Antibacterial action and target mechanisms of zinc oxide nanoparticles
711 against bacterial pathogens. *Sci. Rep.* **12**, 2658 (2022).
- 712 81. Ponce, M. L. & Kleinmann, H. K. The chick chorioallantoic membrane as an in vivo
713 angiogenesis model. *Curr. Protoc. cell Biol.* **18**, 15–19 (2003).
- 714 82. Wysoczynski, M. *et al.* Pro-angiogenic actions of CMC-derived extracellular vesicles rely
715 on selective packaging of angiopoietin 1 and 2, but not FGF-2 and VEGF. *Stem cell Rev.*
716 *reports* **15**, 530–542 (2019).
- 717 83. Mittal, A., Negi, P., Garkhal, K., Verma, S. & Kumar, N. Integration of porosity and bio-
718 functionalization to form a 3D scaffold: cell culture studies and in vitro degradation.
719 *Biomed. Mater.* **5**, 45001 (2010).
- 720 84. Hu, Y., Winn, S. R., Krajbich, I. & Hollinger, J. O. Porous polymer scaffolds surface-
721 modified with arginine-glycine-aspartic acid enhance bone cell attachment and
722 differentiation in vitro. *J. Biomed. Mater. Res. Part A An Off. J. Soc. Biomater. Japanese*
723 *Soc. Biomater. Aust. Soc. Biomater. Korean Soc. Biomater.* **64**, 583–590 (2003).
- 724 85. Wang, W. *et al.* Enhancing the hydrophilicity and cell attachment of 3D printed
725 PCL/graphene scaffolds for bone tissue engineering. *Materials (Basel)*. **9**, 992 (2016).
- 726 86. Rondanelli, M. *et al.* Essentiality of manganese for bone health: An overview and update.
727 *Nat. Prod. Commun.* **16**, 1934578X211016649 (2021).
- 728 87. Wang, C.-Y., Xia, W.-H., Wang, L. & Wang, Z.-Y. Manganese deficiency induces avian
729 tibial dyschondroplasia by inhibiting chondrocyte proliferation and differentiation. *Res. Vet.*
730 *Sci.* **140**, 164–170 (2021).

731

Declaration of interests

The authors declare that they have no known competing financial interests or personal relationships that could have appeared to influence the work reported in this paper.

The authors declare the following financial interests/personal relationships which may be considered as potential competing interests:

Journal Pre-proof